Effect of HNO$_3$ Concentration on the Morphologies and Properties of Bi$_2$WO$_6$ Photocatalyst Synthesized by a Hydrothermal Method

Wenjie Wang, Minna Guo, Dongliang Lu, Weimin Wang * and Zhengyi Fu

State Key Laboratory of Advanced Technology for Materials Synthesis and Processing,
Wuhan University of Technology, Wuhan 430070, China; wangwenjie1992@163.com (W.W.);
alibaba1989.cool@163.com (M.G.); 13871382070@163.com (D.L.); zyfu@whu.edu.cn (Z.F.)
* Correspondence: shswmwang@whut.edu.cn; Tel.: +86-27-8721-5421

Abstract: Bi$_2$WO$_6$ samples were prepared by a hydrothermal method using Bi(NO$_3$)$_3$·5H$_2$O and Na$_2$WO$_4$·2H$_2$O as raw materials. X-ray diffraction (XRD), field-emission scanning electron microscopy (FESEM), Raman and Brunauer–Emmett–Teller (BET) were employed for sample characterization. The photocatalytic activity of the samples was evaluated by the degradation of Rhodamine B under visible-light irradiation. The photocatalytic activity of Bi$_2$WO$_6$, as well as the effect of varying HNO$_3$ concentrations on the morphologies of Bi$_2$WO$_6$, was investigated. The HNO$_3$ concentration significantly affected the structure and morphology of the Bi$_2$WO$_6$. The photocatalytic performance varied with the structure, morphology, and surface area of the Bi$_2$WO$_6$ samples. The results indicated that the H10 sample exhibits uniform morphology and excellent photocatalytic performance; using this sample, the degradation of Rhodamine B reached 96% in 90 min under visible-light irradiation.

Keywords: photocatalysis; Bi$_2$WO$_6$; morphology; degradation; nanosheet

1. Introduction

Over the past decades, photocatalysis has attracted significant attention for the effective utilization of solar energy and the reduction of environmental pollution [1–6]. The degradation of dyes, for instance Rhodamine B (RhB), is a typical test that is used to measure the degradation efficiency and the performance of several photocatalysts such as CeO$_2$, ZnO, Ag$_3$PO$_4$, TiO$_2$ [7–16]. TiO$_2$ is well known as an excellent photocatalyst, attributed to its efficient photocatalytic activity and good chemical stability, as well as its environmentally friendly characteristics [17–22]. However, because of its wide band gap of 3.2 eV, only ultraviolet light (approximately 4% of solar energy) [23–26] can be absorbed, which considerably hinders the practical applications of TiO$_2$. Hence, it is necessary and imperative to develop new visible-light–responsive photocatalysts, which can increase the utilization of solar energy.

Among all photocatalysts, Bi$_2$WO$_6$ is known as a potential photocatalyst with a narrow band gap of 2.7 eV as well as several advantages [27–30], such as excellent light catalytic performance, stable structure, and environmentally friendly characteristics; as one of the simplest Aurivillius oxides, Bi$_2$WO$_6$ has a layered structure composed of (WO$_4$) n^{2n-} octahedrons and (Bi$_2$O$_2$) n^{2n+} sheets [31–34]. The valence-band Bi$_2$WO$_6$ structure is composed of hybrid orbitals of Bi 6s and O 2p, which is more dispersed, thereby benefitting the transfer of photo-induced carriers [35]. Currently, a number of studies have reported on the size and morphology control or modification.

For instance, Zhang has synthesized Bi$_2$WO$_6$ with a novel flower-like superstructure using a hydrothermal method without any surfactant or template [36]. Amano has successfully synthesized

a flake-ball Bi_2WO_6 photocatalyst via a hydrothermal process without using any structure-directing agents, which exhibits excellent photocatalytic properties [37]. Wu has synthesized a Bi_2WO_6 hierarchical nest-like structure using a facile method in the presence of polyvinylpyrrolidone (PVP), composed of aligned higher-order nanoplates [38]. Shang has synthesized a novel Bi_2WO_6 nanocage using colloidal carbon as the template via facile reflux in ethylene glycol [39], which exhibits excellent visible-light–driven photocatalytic efficiency.

However, most of the studies focus on the self-assembly of Bi_2WO_6 sheet units using various methods, and the effect on Bi_2WO_6 basic sheet units during the synthesis process has been seldom reported, especially concerning HNO_3 concentrations. Hence, this study investigated the effect of varying HNO_3 concentrations on the structural morphologies and properties of the Bi_2WO_6 photocatalyst, as well as on the formation mechanism. X-ray diffraction (XRD), field-emission scanning electron microscopy (FESEM), Brunauer–Emmett–Teller (BET), as well as Raman were employed for measuring the crystal structure, morphology, and surface area. In addition, the degradation of Rhodamine B was utilized for evaluating the photocatalytic properties of Bi_2WO_6 prepared at different HNO_3 concentrations.

2. Results

2.1. Structural Analysis

Figure 1 shows the typical XRD patterns observed for the samples, showing their phase structure. All diffraction peaks were assigned to orthorhombic Bi_2WO_6 (JCPDS: 39-256) [40]. Peaks were observed at $28.2°$, $32.7°$, $47.1°$ and $55.9°$, corresponding to the diffraction peaks of the (131), (200), (202), and (133) crystal planes of Bi_2WO_6, respectively. All of the samples clearly exhibited high intensity and narrow diffraction peaks, indicative of the excellent crystallinity of the samples. Meanwhile, the XRD peaks of the samples with HNO_3 (H5, H10, H15) exhibited a slight shift as compared to those observed for the H0 sample (without HNO_3). The larger the diffraction angle, the more obvious the shift. Table 1 shows the average grain size and lattice constant *a* of the samples, which is calculated by Jade 5.0 and the Scherrer equation [41,42].
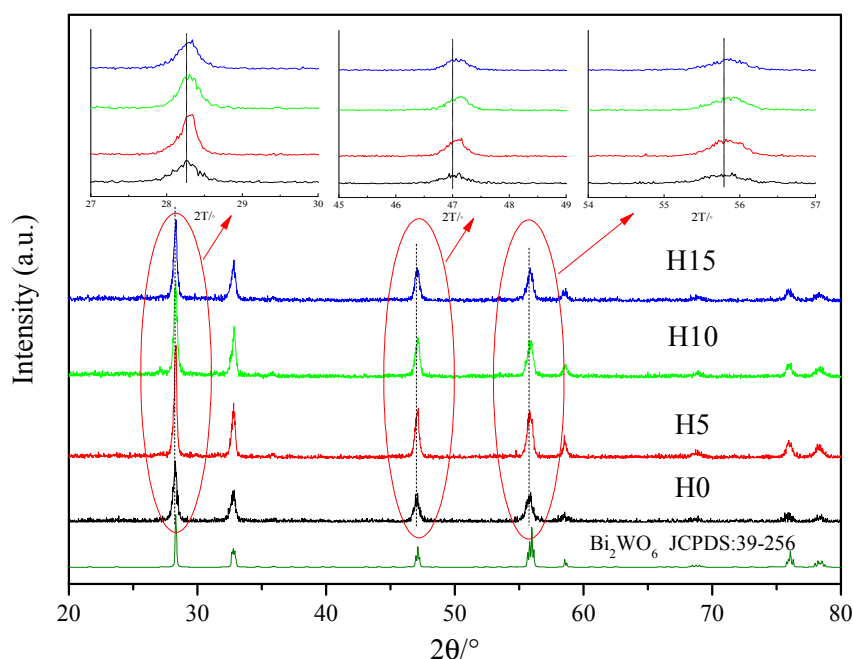
Figure 1. X-ray diffraction (XRD) patterns of Bi_2WO_6 samples prepared by different HNO_3 concentrations. H0, H5, H10, H15 represent the samples prepared by adding 0 mL, 5 mL, 10 mL, 15 mL HNO_3 with certain concentrations (the details can be found in the sample preparation section).

**Table 1.** Grain size and lattice constant of the samples prepared at different HNO_3 concentrations.

Sample	Grain Size/nm	Lattice Constant a/Å
H0	28.3	5.45649
H5	49.0	5.45493
H10	38.3	5.45301
H15	36.0	5.45004

Table 1 shows the average grain size and lattice constant a of the samples. The lattice constant a of the samples decreased with the increasing HNO_3 concentration, attributed to the addition of HNO_3 changing the growth of the Bi_2WO_6 grain, which results in the distortion of the crystal lattice, thereby decreasing the lattice constant.

2.2. Morphologies Analysis

Figure 2 shows the FESEM images of Bi_2WO_6 samples prepared using different HNO_3 concentrations. As shown in Figure 2a, H0 exhibited a two-dimensional (2D) square sheet structure, with a length and width of approximately 1 μm and a thickness of nearly 80 nm. As shown in Figure 2b, the 2D sheet structure was composed of irregular nanosheets, arranged in order. This observation indicated that nanosheets exhibit a strong Van Edward force with each other [43], caused by the fact that although the sample was stirred and subjected to ultrasonic dispersion and centrifugation during preparation, the structure retained its stability. However, after adding a certain amount of HNO_3 (as can be observed in H5), the 2D sheet structure became smaller and more uniform (the length and width were approximately 0.5 μm, and the thickness was 50 nm) (Figure 2c). As shown in Figure 2d, the hierarchical structure of the nanosheet disappeared, and the closely integrated sheet structure became smoother as compared with that in Figure 2b. With increasing HNO_3 concentrations, as shown in Figure 2e,f, the morphology transformed from an irregular size (as can be observed in H5) into a regular square structure, with a length and thickness of approximately 0.15 μm and 40 nm (H10), respectively, and the nano-squares overlapped each other, forming a porous structure. In Figure 2g (H15), with the further increase in the HNO_3 concentration, the morphology of the sample remained the same. Nevertheless, irregular Bi_2WO_6 nanoparticles combined with each other, resulting in considerable sample agglomeration.
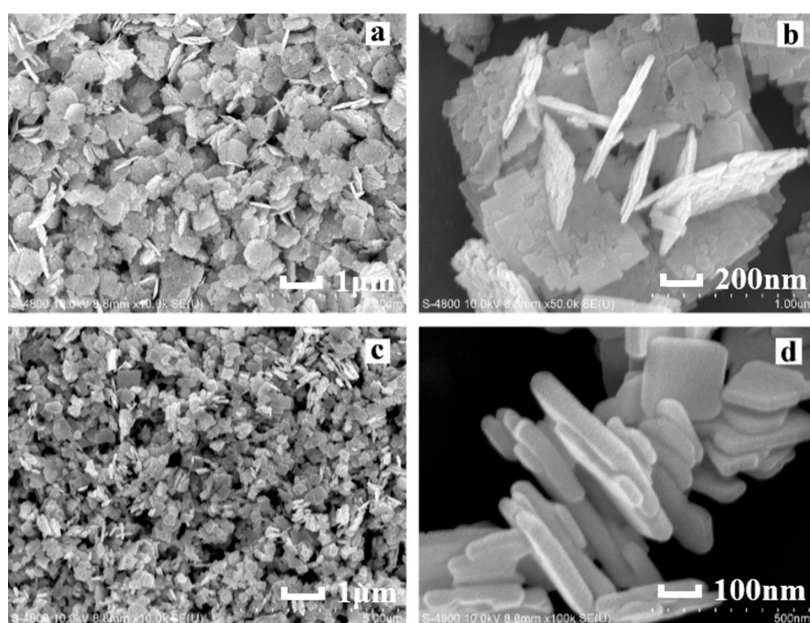

Figure 2. *Cont.*
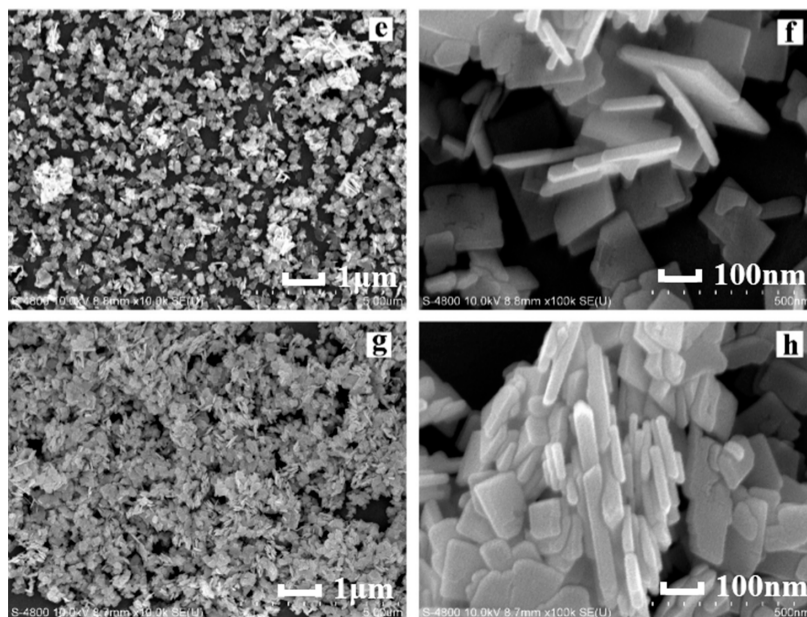
Figure 2. Field-emission scanning electron microscopy (FESEM) images of Bi_2WO_6 samples prepared using different HNO_3 concentrations: (**a**,**b**) H0; (**c**,**d**) H5; (**e**,**f**) H10; (**g**,**h**) H15.

The size of the samples decreased with the increasing HNO_3 concentration. The H^+ concentration increased with the increasing HNO_3 concentration, which accelerates the combination of H^+ and WO_4^{2-}. Hence, an increasing amount of H_2WO_4 precipitates are formed [44], which provide a large number of nucleation centers for Bi_2WO_6; these nucleation centers increase the nucleation rate. However, because of a high number of nucleation centers, ion diffusion is restricted, resulting in a decreased sample size, as well as a more compact structure. The small nanosheets produced during crystallization were mainly attributed to the anisotropy of Bi_2WO_6.

2.3. Raman Analysis

Figure 3 shows the Raman spectra of the samples, which was conducted for characterizing the sample structure. A peak was observed at 713 cm^{-1}, attributed to the asymmetric stretching vibration between the W plane and O atoms [32]. Peaks were also observed at 793 cm^{-1} and 824 cm^{-1}, attributed to the symmetric and asymmetric stretching vibrations between W atoms and O atoms [45]. Peaks were also observed at 170–520 cm^{-1}, mainly attributed to the stretching or bending vibration of the WO_6 octahedron, BiO_6 polyhedron, and Bi–O bonds [46]. The peak observed at 149 cm^{-1} was attributed to the external vibration mode of the WO_6 octahedron [47]. However, a slight red-shift was observed at 149, 713, 793 and 824 cm^{-1} with the characteristic peaks of the Bi_2WO_6 samples prepared by the addition of HNO_3. The addition of HNO_3 results in the decrease of the sample particle size. However, the XRD results indicate that grain size increases after the addition of HNO_3. Hence, the grain-boundary densities decrease, resulting in the decrease of internal stress, as well as the possible weakening of the structural vibration [48,49]; this weakened vibration intensity results in a red-shift of the Raman characteristic peak.
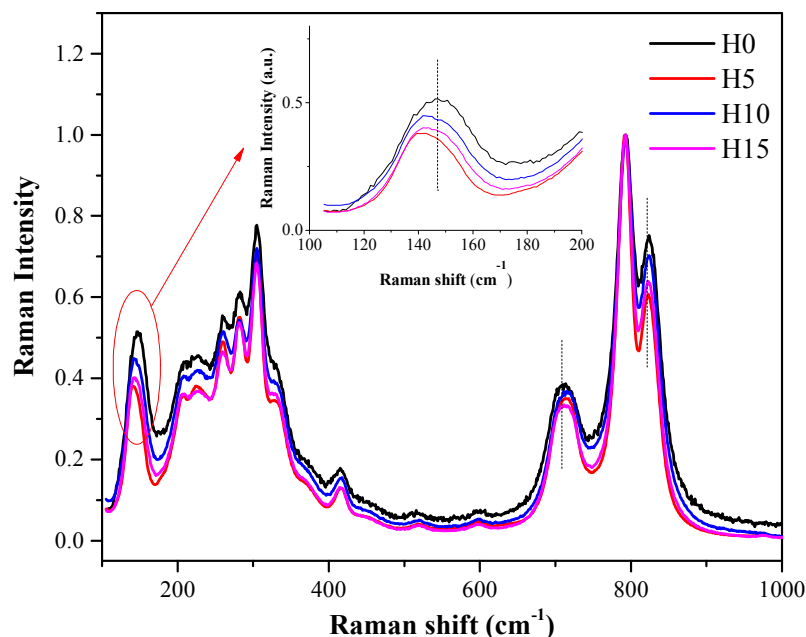
Figure 3. Raman spectra of Bi_2WO_6 samples prepared using different HNO_3 concentrations.

2.4. Surface Area Characterization

Figure 4a,b show the nitrogen adsorption-desorption isotherms of Bi_2WO_6 samples and the pore size distribution curves, respectively. All of the four samples exhibited a type IV isotherm with an H3 hysteresis loop, suggesting that mesopores are formed by the stacking of the flake-like samples, as revealed by SEM images in Figure 2. The greater the amount of mesopores, the higher the BET-specific surface area.
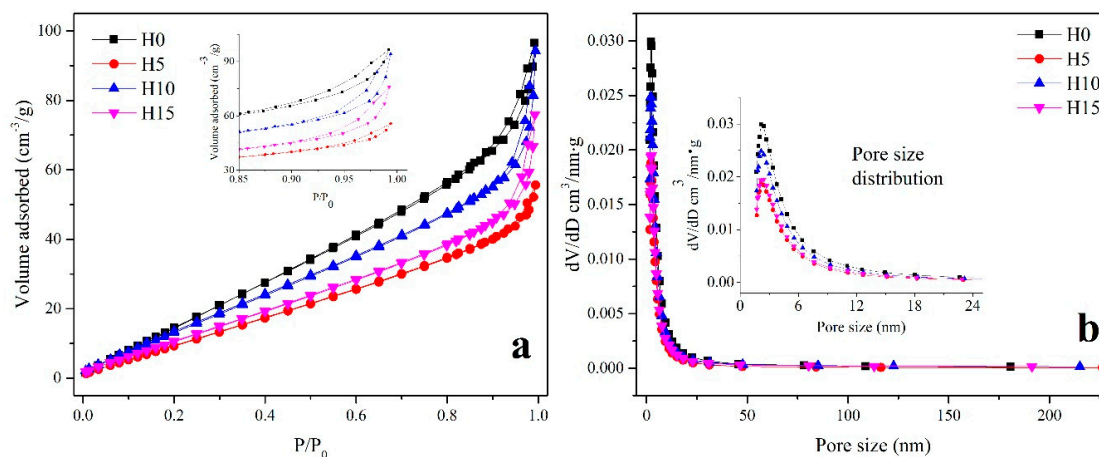
Figure 4. (**a**) Adsorption-desorption isotherms; (**b**) pore size distribution of Bi_2WO_6 samples prepared using different HNO_3 concentrations.

As shown in the details in Table 2, the BET-specific surface area and pore size varied with experimental parameters. The BET surface and Barrett–Joyner–Halenda (BJH) volume exhibited the same tendency with varying experimental parameters. H0 exhibited the largest BET surface (102.16 $m^2 \cdot g^{-1}$) and BJH pore volume (0.18 $cm^3 \cdot g^{-1}$), combined with the SEM results, because the two-dimensional sheet structure of H0 was composed of the small nanoparticles, which resulted in the increase of porosity as well as a large surface area. With the addition of HNO_3, the size of

Bi_2WO_6 decreased, and the superposition of Bi_2WO_6 significantly increased, resulting in a decreasing porosity. Hence, the BET-specific surface area and BJH pore volume decrease to 62.92 $m^2 \cdot g^{-1}$ and 0.11 $cm^3 \cdot g^{-1}$, respectively. With the increasing HNO_3 concentration, a regular square structure was observed. The regular nanosheets were small and overlapped with each other, thereby increasing the porosity between the particles. Thus, H10 exhibits a relatively large pore volume (0.17 $cm^3 g^{-1}$) and a BET surface area (82.33 $m^2 \cdot g^{-1}$). However, the H15 sample exhibited a rather small BET surface area of 65.94 $m^2 \cdot g^{-1}$, attributed to the closely bound, severe aggregation of Bi_2WO_6 nanoplates.

Table 2. BET surface area and pore size of Bi_2WO_6 samples prepared by different HNO_3 concentrations.

Sample	BET Surface/$m^2 \cdot g^{-1}$	BJH Pore Volume/$cm^3 \cdot g^{-1}$	BJH Pore Size/nm
H0	102.16	0.18	5.85
H5	62.92	0.11	5.47
H10	82.33	0.17	7.08
H15	65.94	0.14	7.12

2.5. Photocatalytic Study

The photodegradation of Bi_2WO_6 samples prepared using different HNO_3 concentrations was investigated using Rhodamine B as a pollutant model. As shown in Figure 5a, H0 and H10 exhibited excellent photocatalytic activities, which is much better than those of the TiO_2 (P25) photocatalyst (the green curve). The degradation rate of Rhodamine B reached 96% after 90 min. With the increasing HNO_3 concentration, the photocatalytic performance of the samples first decreased, then increased, and finally decreased. Meanwhile, H10 exhibited the best photocatalytic properties. From the results of XRD, Raman, SEM, and BET, it is obvious that compared with the other samples, the H10 sample has higher crystallinity, more regular morphology, larger specific surface area and pore structure, and these factors make the sample have higher photocatalytic activity [7,50]. Figure 5b shows the absorbance curves of Rhodamine B for H10. The absorption peak observed at 554 nm clearly decreased over time. The initial absorption value of Rhodamine B was 3, while after visible-light irradiation for 90 min, it decreased to almost 0, and the curve nearly became a straight line. No other absorption peaks were observed, indicating that Rhodamine B is almost completely degraded.
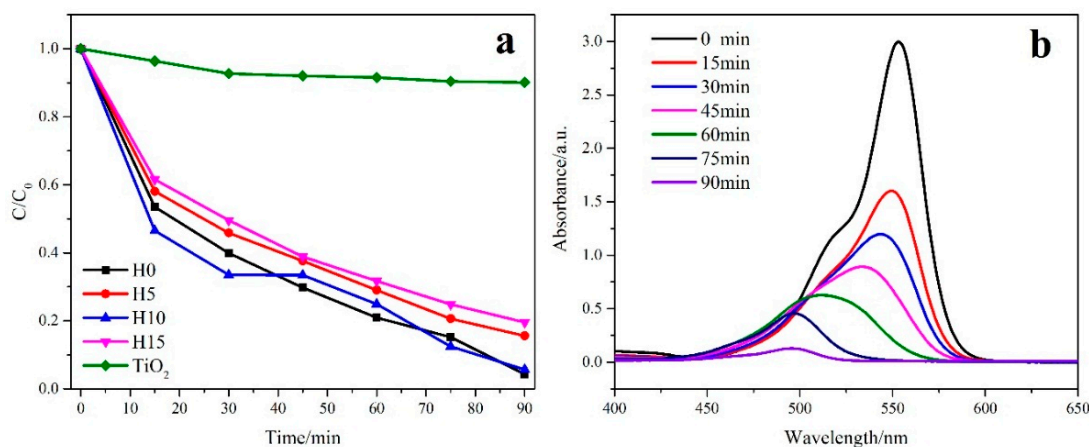
Figure 5. Photocatalytic activity of Bi_2WO_6 samples (**a**) prepared using different HNO_3 concentrations, (**b**) as well as their UV spectrum.

Various primary active species, such as superoxide radicals ($\bullet O_2^-$), hydroxyl radicals ($\bullet OH$), and photogenerated holes (h^+), could be created during the photocatalytic degradation process [10]. It is important to detect the main oxidative species in the photocatalytic mechanism of Bi_2WO_6. In this study, *p*-benzoquinone (BZQ, an $\bullet O_2^-$ radical scavenger, *c* = 2mol/L), disodium ethylene diamine tetra

acetate (Na$_2$-EDTA, a hole scavenger, c = 2mol/L), and *tert*-butanol (*t*-BuOH, an ·OH radical scavenger, c = 2mol/L) were used [51]. As shown in Figure 6, when BZQ, a scavenger for •O$_2^-$ radicals, is added to the H0 and H10 reaction system, an obvious degradation decrease of Rhodamine B is observed. However, for both H0 and H10 samples, the addition of *t*-BuOH, a scavenger for •OH radicals, nearly had no deleterious effect on the photocatalytic activity. While the radical scavenger of Na$_2$-EDTA for h$^+$ is added to the H0 and H10 samples, the degradation of Rhodamine B is both remarkably prohibited (the degradation rate decreases from almost 96% to 39%). These results suggest that the addition of a certain concentration of HNO$_3$ has little influence on the creation of active species and Rhodamine B photodegradation by Bi$_2$WO$_6$ under visible-light is dominated by h$^+$ and •O$_2^-$ oxidation being the main active species. The reason that •OH radicals are not involved in the photocatalytic degradation of Rhodamine B is that •OH might only be formatted via the e$^-$ →O$_2$→H$_2$O$_2$→•OH route [50]. Meanwhile, the standard redox potential of positive holes photogenerated in the valence band of Bi$_2$WO$_6$ is more negative than that of OH/ OH$^-$, suggesting that the "non-selective" •OH radicals could not be formed in the heterogeneous photocatalytic oxidation [52–54].
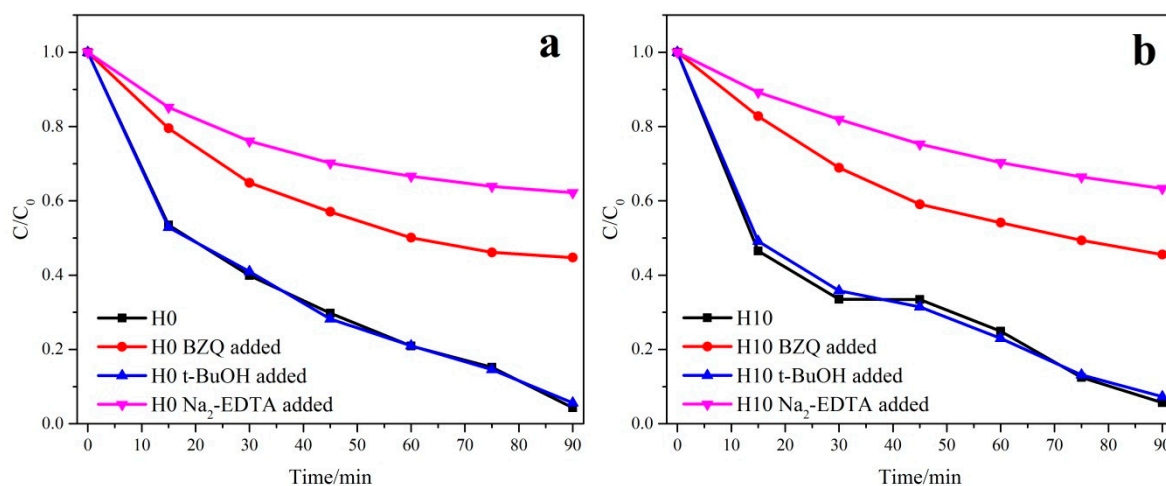
Figure 6. Trapping experiments of photocatalytic degradation of both H0 (**a**) and H10 (**b**) samples with/without the presence of scavengers.

Based on the trapping experiment results, we propose a possible mechanism for the photocatalytic degradation of Bi$_2$WO$_6$. Under visible-light irradiation, electro-hole pairs are generated over the semiconductor Bi$_2$WO$_6$ in water and the photogenerated electrons trapped with molecular oxygen would further produce •O$_2^-$ radicals. The adsorbed Rhodamine B on the surface of Bi$_2$WO$_6$ is oxidized by the h$^+$ and •O$_2^-$ radicals.

3. Materials and Methods

3.1. Sample Preparation

Bi$_2$WO$_6$ was prepared by the hydrothermal method using Bi(NO$_3$)$_3$·5H$_2$O and Na$_2$WO$_4$·2H$_2$O as the raw materials. First, 4 mmol Bi(NO$_3$)$_3$·5H$_2$O and 2 mmol Na$_2$WO$_4$·2H$_2$O were dissolved in 40 mL and 20 mL deionized water, respectively. Second, the precursor was obtained after mixing the two solutions. HNO$_3$ and NaOH were used for adjusting the pH of the precursor and the final pH value was 3. Third, the precursor was transferred into a 100 mL stainless steel Teflon-lined autoclave, which was maintained at 160 °C for 12 h, and then naturally cooled to room temperature. Next, the sample was washed several times using deionized water and absolute ethanol and then dried at 60 °C for 12 h. Maintaining the other conditions constant, Bi(NO$_3$)$_3$·5H$_2$O was dissolved in 40 mL HNO$_3$ (HNO$_3$ solution was prepared by HNO$_3$ (c = 8 mol/L) with contents of 5 mL, 10 mL, 15 mL), the above

steps were repeated for each sample. Hereafter, the samples will be referred to as H0, H5, H10, and H15 by the addition of 0 mL, 5 mL, 10 mL, and 15 mL of the HNO_3 solution, respectively.

3.2. Sample Characterization

X-Ray diffraction (XRD) patterns were recorded on a DlmaxUltimaIII (Rigaku Corporation, Tokyo, Japan) with CuKα1 radiation under 40 kV and 40 mA, with scanning over a range of 20°–80°. The morphology and size of the samples were investigated by scanning electron microscopy (SEM) (S-3400N, HITACHI Corporation, Tokyo, Japan). The Brunauer–Emmett–Teller (BET) surface area was estimated in terms of the N_2 adsorption data using a volumetric adsorption apparatus (ASAP 2020 HD88, Micromeritics Corporation, Norcross, GA, USA). The concentration of the remnant Rhodamine B was monitored on a UV–vis spectrophotometer (UV-2550, Shimadzu Corporation, Kyoto, Japan). For evaluating the photocatalytic activities of the samples (50 mg), the degradation of Rhodamine B (50 mL; 20 mg/L) under visible light was investigated using a 300 W Xe lamp with a cut-off filter having a wavelength of 420 nm. The degradation experiment was conducted at three times, and the results in Figure 5a represent the average values of the three measurements.

4. Conclusions

In summary, Bi_2WO_6 samples were prepared using different HNO_3 concentrations by a hydrothermal method. The results reveal that the HNO_3 concentration affects the structure, morphology, and photocatalytic performance of the samples. The XRD and Raman peaks of the samples exhibited slight shifts with the addition of HNO_3, indicating the changes of grain size and structure. Meanwhile, the morphology of Bi_2WO_6 becomes more compact with the increasing HNO_3 concentration, and the BET surface area was consistent with the SEM results, while a further increase in the HNO_3 concentration resulted in the considerable aggregation of Bi_2WO_6. Thus, both the structure and morphology significantly affect the photocatalytic performance of the samples. UV-vis measurements imply that H10 exhibits the best photocatalytic properties, and its degradation of Rhodamine B can reach 96% after 90 min. The addition of HNO_3 has little influence on the creation of active species and Rhodamine B photodegradation by Bi_2WO_6 under visible-light is dominated by h^+ and $\bullet O_2^-$ oxidation being the main active species.

Author Contributions: Weimin Wang conceived and designed the experiments; Dongliang Lu and Wenjie Wang performed the experiments; Minna Guo and Wenjie Wang analyzed the data; Zhengyi Fu contributed reagents/materials/analysis tools; Wenjie Wang wrote the paper.

Conflicts of Interest: The authors declare no conflict of interest.

Abbreviations

The following abbreviations are used in this manuscript:

XRD	X-ray diffraction
SEM	Scanning electron microscopy
BET	Brunauer–Emmett–Teller
BJH	Barrett–Joyner–Halenda

References

1. Zhang, Q.; Liu, Y.; Bu, X.; Wu, T.; Feng, P. A rare (3, 4)-connected chalcogenide superlattice and its photoelectric effect. *Angew. Chem. Int. Ed.* **2008**, *47*, 113–116. [CrossRef] [PubMed]
2. Gao, J.; Miao, J.; Li, P.Z.; Teng, W.Y.; Yang, L.; Zhao, Y.; Liu, B.; Zhang, Q. A p-type Ti (iv)-based metal–organic framework with visible-light photo-response. *Chem. Commun.* **2014**, *50*, 3786–3788. [CrossRef] [PubMed]

3. Liu, Y.; Kanhere, P.D.; Wong, C.L.; Tian, Y.; Feng, Y.; Boey, F.; Wu, T.; Chen, H.; White, T.J.; Chen, Z.; et al. Hydrazine-hydrothermal method to synthesize three-dimensional chalcogenide framework for photocatalytic hydrogen generation. *J. Solid State Chem.* **2010**, *183*, 2644–2649. [CrossRef]

4. Gao, J.; Cao, S.; Tay, Q.; Liu, Y.; Yu, L.; Ye, K.; Mun, P.C.S.; Li, Y.; Rakesh, G.; Chye, S.; et al. Molecule-Based Water-Oxidation Catalysts (WOCs): Cluster-Size-Dependent Dye-Sensitized Polyoxometalates for Visible-Light-Driven O_2 Evolution. *Sci. Rep.* **2013**, *3*. [CrossRef] [PubMed]

5. Liao, Y.H.B.; Wang, J.X.; Lin, J.S.; Chung, W.-H.; Lin, W.-Y.; Chen, C.-C. Synthesis, photocatalytic activities and degradation mechanism of Bi_2WO_6 toward crystal violet dye. *Catal. Today* **2011**, *174*, 148–159. [CrossRef]

6. Fan, H.J.; Lu, C.S.; Lee, W.L.W.; Chiou, M.-R.; Chen, C.-C. Mechanistic pathways differences between P25-TiO_2 and Pt-TiO_2 mediated CV photodegradation. *J. Hazard. Mater.* **2011**, *185*, 227–235. [CrossRef] [PubMed]

7. Huang, S.T.; Jiang, Y.R.; Chou, S.Y.; Dai, Y.-M.; Chen, C.-C. Synthesis, characterization, photocatalytic activity of visible-light-responsive photocatalysts BiO_xCl_y/BiO_mBr_n by controlled hydrothermal method. *J. Mol. Catal. A Chem.* **2014**, *391*, 105–120. [CrossRef]

8. Lin, H.P.; Lee, W.W.; Huang, S.T.; Chen, L.-W.; Yeh, T.-W.; Fu, J.-Y.; Chen, C.-C. Controlled hydrothermal synthesis of $PbBiO_2Br/BiOBr$ heterojunction with enhanced visible-driven-light photocatalytic activities. *J. Mol. Catal. A Chem.* **2016**, *417*, 168–183. [CrossRef]

9. Lee, W.L.W.; Huang, S.T.; Chang, J.L.; Chen, J.-Y.; Cheng, M.-C. Photodegradation of CV over nanocrystalline bismuth tungstate prepared by hydrothermal synthesis. *J. Mol. Catal. A Chem.* **2012**, *361*, 80–90. [CrossRef]

10. Lin, H.P.; Chen, C.C.; Lee, W.W.; Lai, Y.-Y.; Chen, J.-Y.; Chen, Y.-Q.; Fu, J.-Y. Synthesis of a $SrFeO_{3-x}/g$-C_3N_4 heterojunction with improved visible-light photocatalytic activities in chloramphenicol and crystal violet degradation. *RSC Adv.* **2016**, *6*, 2323–2336. [CrossRef]

11. Chou, S.Y.; Chen, C.C.; Dai, Y.M.; Lin, J.-H.; Lee, W.W. Novel synthesis of bismuth oxyiodide/graphitic carbon nitride nanocomposites with enhanced visible-light photocatalytic activity. *RSC Adv.* **2016**, *6*, 33478–33491. [CrossRef]

12. Yang, C.T.; Lee, W.W.; Lin, H.P.; Dai, Y.-M.; Chi, H.-T.; Chen, C.-C. A novel heterojunction photocatalyst, Bi_2SiO_5/g-C_3N_4: Synthesis, characterization, photocatalytic activity, and mechanism. *RSC Adv.* **2016**, *6*, 40664–40675. [CrossRef]

13. Li, C.; Chen, R.; Zhang, X.; SHU, S.; Xiong, J.; Zheng, Y.; Dong, W. Electrospinning of CeO_2–ZnO composite nanofibers and their photocatalytic property. *Mater. Lett.* **2011**, *65*, 1327–1330. [CrossRef]

14. Yang, S.J.; Im, J.H.; Kim, T.; Lee, K.; Park, C.R. MOF-derived ZnO and ZnO@ C composites with high photocatalytic activity and adsorption capacity. *J. Hazard. Mater.* **2011**, *186*, 376–382. [CrossRef] [PubMed]

15. Li, H.; Yin, S.; Wang, Y.; Sekino, T.; Lee, S.W.; Sato, T. Green phosphorescence-assisted degradation of rhodamine B dyes by Ag_3PO_4. *J. Mater. Chem. A* **2013**, *1*, 1123–1126. [CrossRef]

16. Li, H.; Zhang, W.; Li, B.; Pan, W. Diameter-dependent photocatalytic activity of electrospun TiO_2 nanofiber. *J. Am. Ceram. Soc.* **2010**, *93*, 2503–2506. [CrossRef]

17. Frank, S.N.; Bard, A.J. Heterogeneous Photocatalytic Oxidation of Cyanide and Sulfite in Aqueous Solutions at Semiconductor Powders. *J. Phys. Chem.* **1977**, *81*, 1484–1488. [CrossRef]

18. Li, Y.; Fang, X.; Koshizaki, N.; SASAKI, T.; Li, L.; Gao, S.; Shimizu, Y.; Bando, Y.; Golberg, D. Periodic TiO_2 nanorod arrays with hexagonal nonclose-packed arrangements: Excellent field emitters by parameter optimization. *Adv. Funct. Mater.* **2009**, *19*, 2467–2473. [CrossRef]

19. Collins, J.J.; Bodner, K.; Aylward, L.L.; Wilken, M.; Bodnar, C.M. Mortality rates among trichlorophenol workers with exposure to 2, 3, 7, 8-tetrachlorodibenzo-*p*-dioxin. *Am. J. Epidemiol.* **2009**, *170*, 501–506. [CrossRef] [PubMed]

20. Shen, J.M.; Chen, Z.L.; Xu, Z.Z.; Li, X.Y.; Xu, B.B.; Qi, F. Kinetics and mechanism of degradation of p—Chloronitrobenzene in water by ozonation. *J. Hazard. Mater.* **2008**, *152*, 1325–1331. [CrossRef] [PubMed]

21. Sharma, S.; Mukhopadhyay, M.; Murthy, Z.V.P. Degradation of 4-Chlorophenol in Wastewater by Organic Oxidants. *Ind. Eng. Chem. Res.* **2010**, *49*, 3094–3098. [CrossRef]

22. Hu, M.; Xu, Y. Visible light induced degradation of chlorophenols in the presence of H_2O_2 and iron substituted polyoxotungstate. *Chem. Eng. J.* **2014**, *246*, 299–305. [CrossRef]

23. Pera-Titus, M.; GarciA-Molina, V.; Baños, M.A.; Gimenez, J.; Esplugas, S. Degradation of chlorophenols by means of advanced oxidation processes: A general review. *Appl. Catal. B Environ.* **2004**, *47*, 219–256. [CrossRef]

24. Yue, L.; Takeshi, S.; Yoshiki, S.; Koshizaki, N. A hierarchically ordered TiO_2 hemispherical particle array with hexagonal-non-close-packed tops: Synthesis and stable superhydrophilicity without UV irradiation. *Small* **2008**, *4*, 2286–2291.

25. Fujishima, A.; Honda, K. Electrochemical photolysis of water at a semiconductor electrode. *Nature* **1972**, *238*, 37–38. [CrossRef] [PubMed]

26. Jimmy, C.Y.; Zhang, L.; Zheng, Z.; Zhao, J. Synthesis and Characterization of Phosphated Mesoporous Titanium Dioxide with High Photocatalytic Activity. *Chem. Mater.* **2003**, *15*, 2280–2286.

27. Zhang, S.; Zhang, C.; Man, Y.; Zhu, Y. Visible-light-driven photocatalyst of Bi_2WO_6 nanoparticles prepared via amorphous complex precursor and photocatalytic propertie. *J. Solid State Chem.* **2006**, *179*, 62–69. [CrossRef]

28. Zhang, L.; Wang, W.; Zhou, L.; Xu, H. Bi_2WO_6 Nano- and Microstructures: Shape Control and Associated Visible-Light-Driven Photocatalytic Activities. *Small* **2007**, *3*, 1618–1625. [CrossRef] [PubMed]

29. Kudo, A.; Hijii, S. H_2 or O_2 Evolution from Aqueous Solutions on Layered Oxide Photocatalysts Consisting of Bi with 6s2 Configuration and d0 Transition Metal Ions. *Chem. Lett.* **1999**, *28*, 1103–1104. [CrossRef]

30. Yu, J.; Kudo, A. Hydrothermal Synthesis and Photocatalytic Property of 2Dimensional Bismuth Molybdate Nanoplates. *Chem. Lett.* **2005**, *34*, 1528–1529. [CrossRef]

31. Fu, H.; Pan, C.; Yao, W.; Zhu, Y. Visible-light-induced degradation of rhodamine B by nanosized Bi_2WO_6. *J. Phys. Chem. B* **2005**, *109*, 22432–22439. [CrossRef] [PubMed]

32. Fu, H.; Zhang, L.; Yao, W.; Zhu, Y. Photocatalytic properties of nanosized Bi_2WO_6 catalysts synthesized via a hydrothermal process. *Appl. Catal. B Environ.* **2006**, *66*, 100–110. [CrossRef]

33. Kim, N.; Vannier, R.N.; Grey, C.P. Detecting different oxygen-ion jump pathways in Bi_2WO_6 with 1-and 2-dimensional 17O MAS NMR spectroscopy. *Chem. Mater.* **2005**, *17*, 1952–1958. [CrossRef]

34. Tang, J.; Zou, Z.; Ye, J. Photocatalytic Decomposition of Organic Contaminants by Bi_2WO_6 under Visible Light Irradiation. *Catal. Lett.* **2003**, *92*, 53–56. [CrossRef]

35. Lu, L.; Kobayashi, A.; Tawa, K.; Ozaki, Y. Silver nanoplates with special shapes: Controlled synthesis and their surface plasmon resonance and surface-enhanced Raman scattering properties. *Chem. Mater.* **2006**, *18*, 4894–4901. [CrossRef]

36. Zhang, L.; Wang, W.; Chen, Z.; Zhou, L.; Xu, H.; Zhu, W. Fabrication of flower-like Bi_2WO_6 superstructures as high performance visible-light driven photocatalysts. *J. Mater. Chem.* **2007**, *17*, 2526–2532. [CrossRef]

37. Amano, F.; Nogami, K.; Abe, R.; Ohtani, B. Preparation and characterization of bismuth tungstate polycrystalline flake-ball particles for photocatalytic reactions. *J. Phys. Chem. C* **2008**, *112*, 9320–9326. [CrossRef]

38. Wu, J.; Duan, F.; Zheng, Y.; Xie, Y. Synthesis of Bi_2WO_6 nanoplate-built hierarchical nest-like structures with visible-light-induced photocatalytic activity. *J. Phys. Chem. C* **2007**, *111*, 12866–12871. [CrossRef]

39. Shang, M.; Wang, W.; Xu, H. New Bi_2WO_6 nanocages with high visible-light-driven photocatalytic activities prepared in refluxing EG. *Cryst. Growth Des.* **2008**, *9*, 991–996. [CrossRef]

40. Zellmer, L.A.; Smith, D.K.; Nelson, D.; Scheetz, B.E. Synthesis and Unit Cell Parameter Refinement of 25 Tungsten Bronze Ferroelectrics. *Powder Diffr.* **1988**, *3*, 222–233. [CrossRef]

41. Drits, V.; Srodon, J.; Eberl, D.D. XRD measurement of mean crystallite thickness of illite and illite/smectite: Reappraisal of the Kubler index and the Scherrer equation. *Clays Clay Mineral.* **1997**, *45*, 461–475. [CrossRef]

42. Burton, A.W.; Ong, K.; Rea, T. On the estimation of average crystallite size of zeolites from the Scherrer equation: A critical evaluation of its application to zeolites with one-dimensional pore systems. *Microporous Mesoporous Mater.* **2009**, *117*, 75–90. [CrossRef]

43. Margenau, H. Van der Waals Forces. *Rev. Mod. Phys.* **1939**, *11*, 1. [CrossRef]

44. Zhou, Y.; Huang, J.; Cao, L. Influence of W/Bi Mole Ratio on Morphology and Optical Property of Bi_2WO_6 Microcrystalline. *J. Chin. Ceram. Soc.* **2012**, *40*, 916–921.

45. Obregón, S.; Colón, G. Erbium doped TiO_2–Bi_2WO_6 heterostructure with improved photocatalytic activity under sun-like irradiation. *Appl. Catal. B Environ.* **2013**, *s140–141*, 299–305. [CrossRef]

46. Zhou, Y.; Antonova, E.; Lin, Y. *In Situ* X-ray Absorption Spectroscopy/Energy-Dispersive X-ray Diffraction Studies on the Hydrothermal Formation of $Bi_2W_{1-x}Mo_xO_6$ Nanomaterials. *Ber. Der Dtsch. Chem. Ges.* **2012**, *5*, 783–789. [CrossRef]

47. Gui, M.S.; Zhang, W.D. Preparation and modification of hierarchical nanostructured Bi_2WO_6 with high visible light-induced photocatalytic activity. *Nanotechnology* **2011**, *22*, 265601. [CrossRef] [PubMed]

48. Zhang, W.J.; Matsumoto, S. Investigations of crystallinity and residual stress of cubic boron nitride films by Raman spectroscopy. *Solid State Commun.* **2001**, *63*, 247–250. [CrossRef]

49. Rats, D.; Bimbault, L.; Vandenbulcke, L.; Herbin, R.; Badawi, K.F. Crystalline quality and residual stresses in diamond layers by Raman and x-ray diffraction analyses. *J. Appl. Phys.* **1995**, *78*, 4994–5001. [CrossRef]

50. Lee, W.W.; Lu, C.S.; Chuang, C.W.; Chen, Y.-J.; Fu, J.-Y.; Siao, C.W.; Chen, C.-C. Synthesis of bismuth oxyiodides and their composites: Characterization, photocatalytic activity, and degradation mechanisms. *RSC Adv.* **2015**, *5*, 23450–23463. [CrossRef]

51. Guo, M. Enhanced photocatalytic activity of S-doped $BiVO_4$ photocatalysts. *Rsc Adv.* **2015**, *5*, 58633–58639. [CrossRef]

52. Zhang, Y.; Zhang, N.; Tang, Z.R.; Xu, Y.-J. Identification of Bi_2WO_6 as a highly selective visible-light photocatalyst toward oxidation of glycerol to dihydroxyacetone in water. *Chem. Sci.* **2013**, *4*, 1820–1824. [CrossRef]

53. Zhang, M.; Chen, C.; Ma, W.; Zhao, J. Visible-Light-Induced Aerobic Oxidation of Alcohols in a Coupled Photocatalytic System of Dye-Sensitized TiO_2 and TEMPO. *Angew. Chem.* **2008**, *120*, 9876–9879. [CrossRef]

54. Zhang, Y.; Zhang, N.; Tang, Z.R.; Xu, Y.J. Transforming CdS into an efficient visible light photocatalyst for selective oxidation of saturated primary C–H bonds under ambient conditions. *Chem. Sci.* **2012**, *3*, 2812–2822. [CrossRef]